Supporting Information

Coordination modulation of single-atom Zn sites to boost oxygen reduction performance

Siying Zhang,[‡ab] Xue Bai,[‡a] Tianmi Tang,[a] Weidong Ruan*[b] and Jingqi Guan*[a]

[a] Institute of Physical Chemistry, College of Chemistry, Jilin University, 2519 Jiefang Road, Changchun 130021, P. R. China. *E-mail guanjq@jlu.edu.cn (J.Q. Guan)

[b] State Key Laboratory of Supramolecular Structure and Materials, College of Chemistry, Jilin University, Changchun 130012, P. R. China. *E-mail: ruanwd@jlu.edu.cn (W.D. Ruan)

‡ Siying Zhang and Xue Bai contributed equally to this work.

1. Materials preparation

100 mg of graphene oxide (GO) was dispersed into 50 mL of distilled water by ultrasonic treatment for 1 h, and then 3.7 mg of $ZnNO_3$ $6H_2O$ was added. The mixture was dried by a rotary evaporator to obtain Zn-GO powder, which was mixed with melamine and then rapidly calcined in a tube furnace for 3 minutes in N_2 atmosphere. The c-Zn-NG-T samples were prepared with different zinc contents (c = 0.3, 0.5, 0.8, or 1.0 wt.%) at different temperatures (T = 700, 800, and 900 °C). T For simplification, 0.8 wt.%-Zn-NG-800 °C was also denoted as Zn-NG. The contrast samples G, NG, and Zn-G were also synthesized using a similar method.

2. Structural characterization of catalysts

X-ray diffraction (XRD) patterns of powder were obtained using a Shimadzu XRD-6000. An instrument used for high angle annular dark field imaging (HAADF) was a JEM-ARM 200 F microscope. Spectra from X-ray photoelectron spectroscopy (XPS) were recorded using a Thermo VG ESCALAB 250. The BL11B beamline of the Shanghai Synchrotron Radiation Facility was used to perform the X-ray absorption spectroscopy (XAS) spectrum of Zn-NG near the Zn K edge.

3. Electrocatalytic measurements

All electrochemical tests are performed on a rotating disk electrode (RDE) controller connected to an electrochemical workstation (CHI760E). Electrochemical tests were performed using a three-electrode system. A saturated calomel electrode (SCE) was used as the reference electrode, a platinum wire was used as the counter electrode, and the catalyst-coated glassy carbon electrode (GCE) was used as the working electrode. The catalyst loading is 0.5 mg cm^{-2}. The electron transfer number (n) determined by the slope of the spectral line is calculated using the K-L equation.[1] The H_2O_2 yield and electron transfer number measured by the rotating ring-disk electrode were calculated by the formula (1) and (2):

$$n = 4 \times \frac{I_d}{I_d + (I_r/N)} \quad (1)$$

$$H_2O_2\% = 200 \times \frac{I_r/N}{I_d + (I_r/N)} \quad (2)$$

I_d and I_r are disk current and ring current, respectively. N is the H_2O_2 collection efficiency of Pt ring, which is 0.25.

4. Zn-air battery measurements

The Zn-air battery performance was evaluated in 6 M KOH on a battery test system (LANHE CT2001A). The modified carbon paper (catalyst loading: 1 mg cm^{-2}) and a Zn plate (1 mm in thickness) were used as the air electrode and the metal electrode, respectively. The electrolyte was a mixture of 6 M KOH and 0.2 M $Zn(Ac)_2$. Catalyst ink was prepared by mixing 100 μL of 1% Nafion/ethanol solution, 500 μL of ethanol and 2 mg catalyst. OCV and discharge polarization curves were measured using a CHI 760E electrochemical workstation. The discharge curves at different current densities (5, 10, 25, and 50 mA cm^{-2}), specific capacity test at 5 mA cm^{-2} and charge-discharge cycle stability test at 5 mA cm^{-2} (each charge-discharge cycle lasts for 20 min) were carried out on LANHE battery test system.

5. Computational methods

Vienna ab initio simulation package (VASP) was employed for the DFT calculations. The exchange-correlation functional was performed using the projector-augmented wave (PAW) method and Perdew-Burke-Ernzerhof (PBE) potential. The Brillouin zone consists of 3 × 3 × 1 Monkhorst-Pack mesh points. The Nørskov's model was used to explore the ORR mechanism. This approach allowed for detailed and accurate calculation of reaction barriers across different material groups. By comparing these barriers, we could assess the ORR efficiency, thus shedding light on their catalytic behaviors and potential applications.

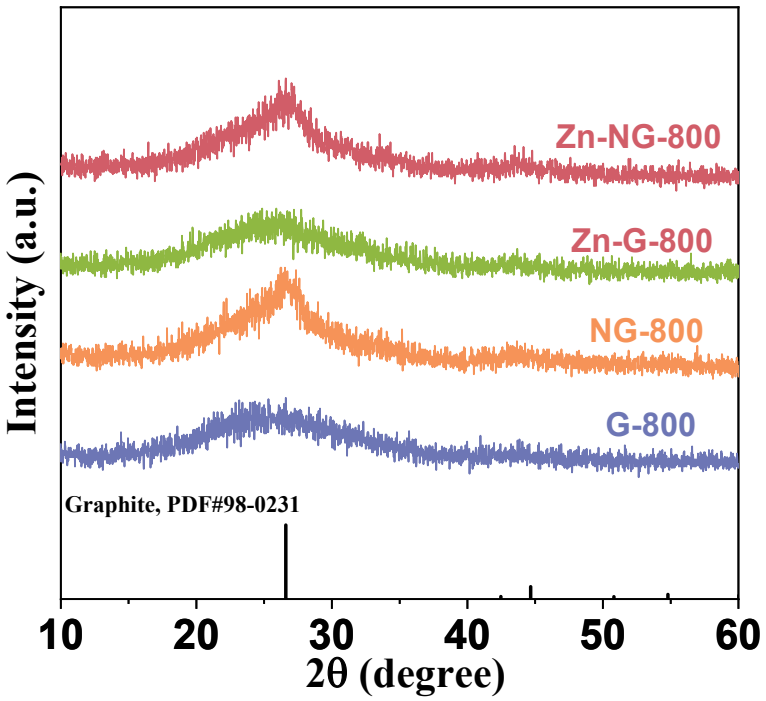

Fig. S1 XRD patterns of Zn-NG-800, Zn-G-800, NG-800 and G-800.

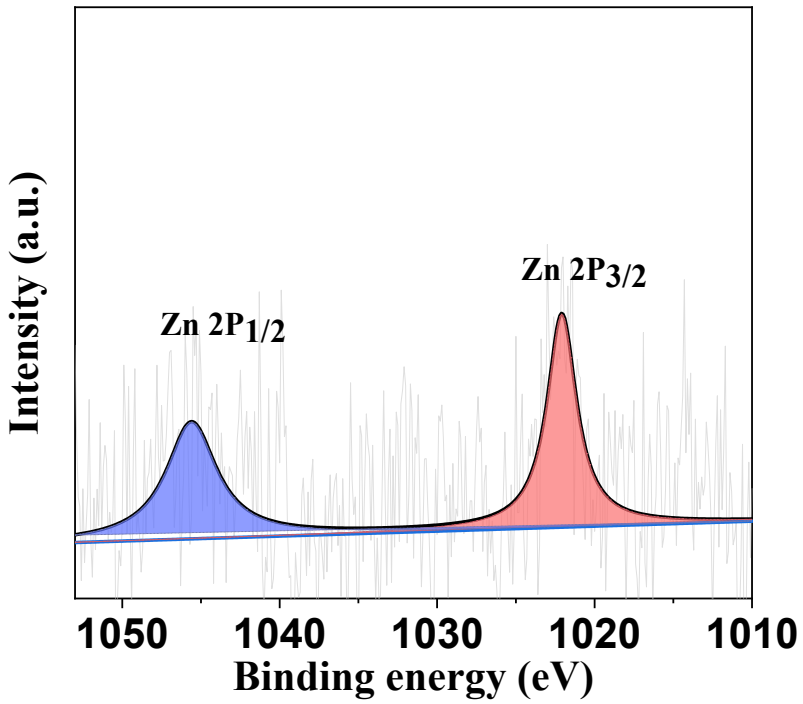

Fig. S2 High Resolution XPS Spectra of Zn 2p

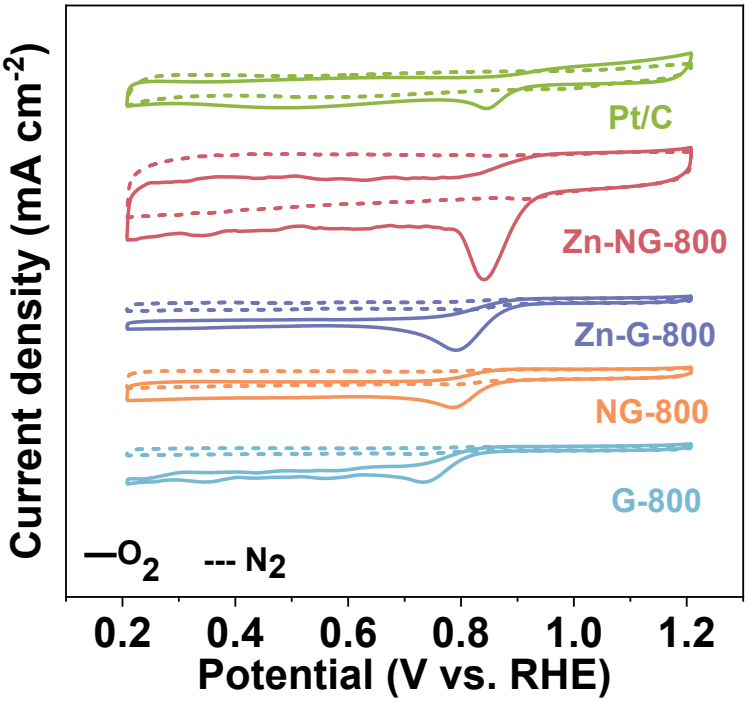

Fig. S3 CV curves of Zn-NG-800, Zn-G-800, NG-800, G-800 and Pt/C in O_2-saturated (solid line) or N_2-saturated (dashed line) 0.1M KOH at a sweep rate of 5 mV s^{-1}.

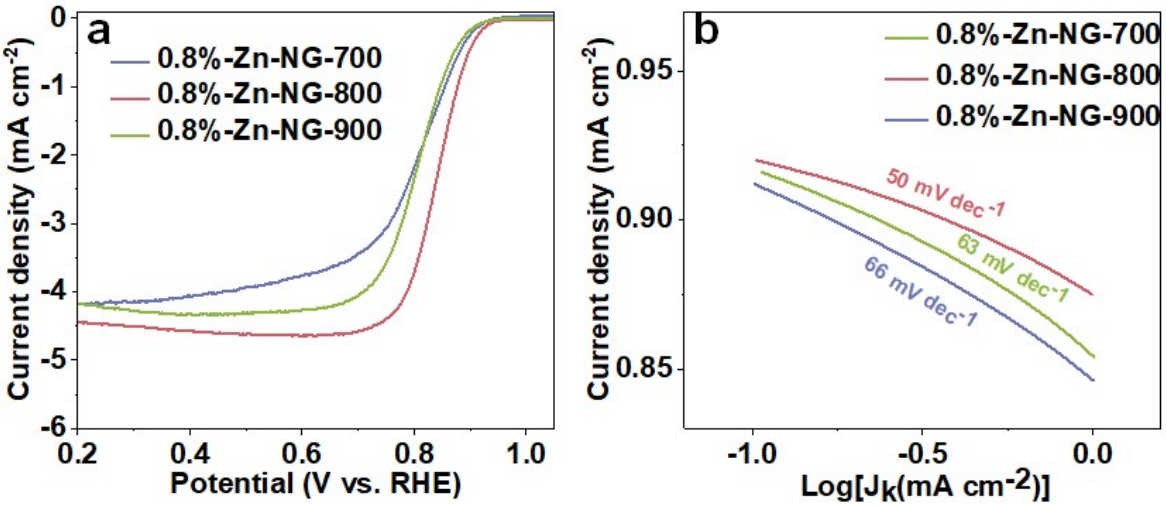

Fig. S4 (a) LSV curves of 0.8% Zn-NG. (b) Tafel plots.

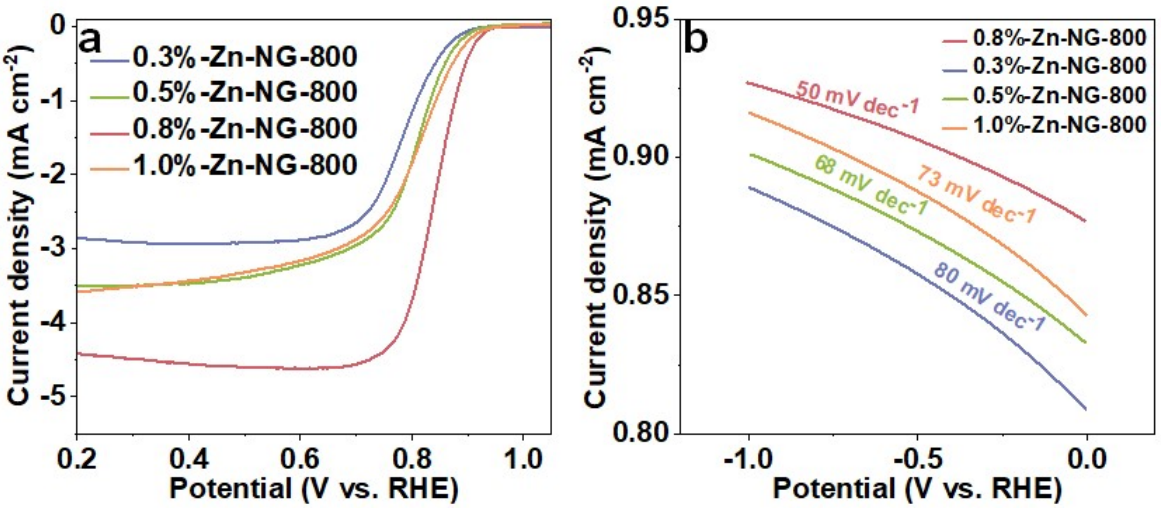

Fig. S5 (a) LSV curves of Zn-NG -800 with different initial Zn contents. (b) Tafel plots.

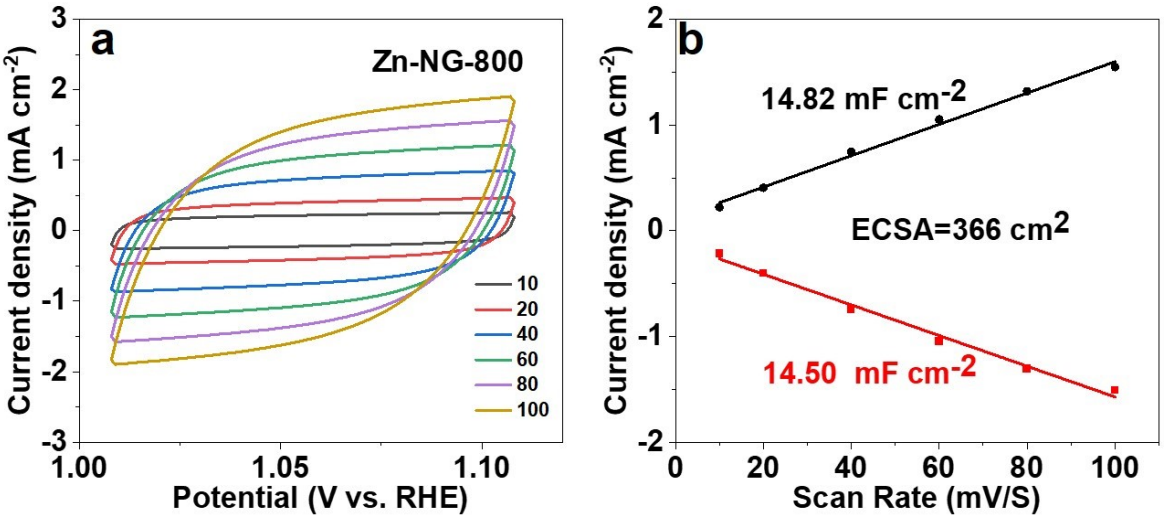

Fig. S6 Double-layer capacitance measurements for determining the electrochemical active surface area for the Zn-NG-800 (a) CVs measured in a non-Faradaic region at scan rate of 10 mV s^{-1}, 20 mV s^{-1}, 40 mV s^{-1}, 60 mV s^{-1}, 80 mV s^{-1}, and 100 mV s^{-1}. (b) The cathodic (black) and anodic (red) currents measured at 1.059 V vs RHE as a function of the scan rate. The average of the absolute value of the slope is taken as the double-layer capacitance of the electrode.

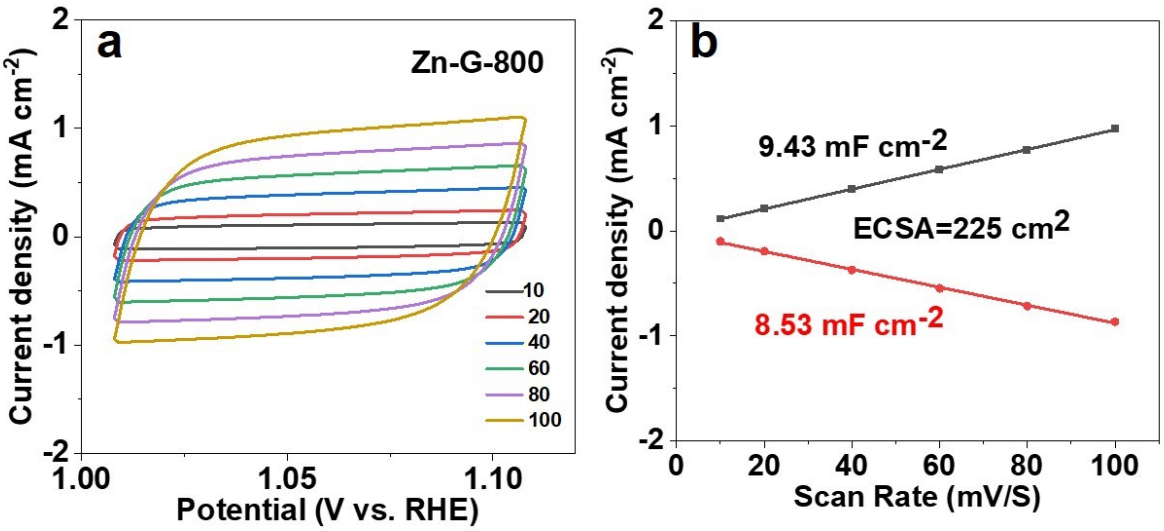

Fig. S7 Double-layer capacitance measurements for determining the electrochemical active surface area for the Zn-G-800. (a) CVs measured in a non-Faradaic region at scan rate of 10 mV s^{-1}, 20 mV s^{-1}, 40 mV s^{-1}, 60 mV s^{-1}, 80 mV s^{-1}, and 100 mV s^{-1}. (b) The cathodic (black) and anodic (red) currents measured at 1.059 V vs RHE as a function of the scan rate. The average of the absolute value of the slope is taken as the double-layer capacitance of the electrode.

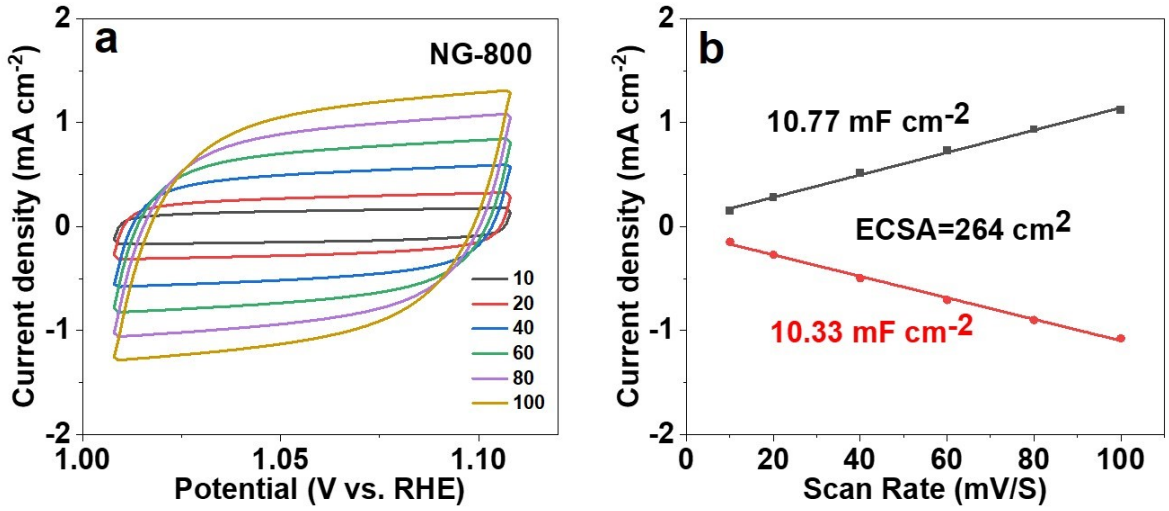

Fig. S8 Double-layer capacitance measurements for determining the electrochemical active surface area for the NG-800. (a) CVs measured in a non-Faradaic region at scan rate of 10 mV s^{-1}, 20 mV s^{-1}, 40 mV s^{-1}, 60 mV s^{-1}, 80 mV s^{-1}, and 100 mV s^{-1}. (b) The cathodic (black) and anodic (red) currents measured at 1.059 V vs RHE as a function of the scan rate. The average of the absolute value of the slope is taken as the double-layer capacitance of the electrode.

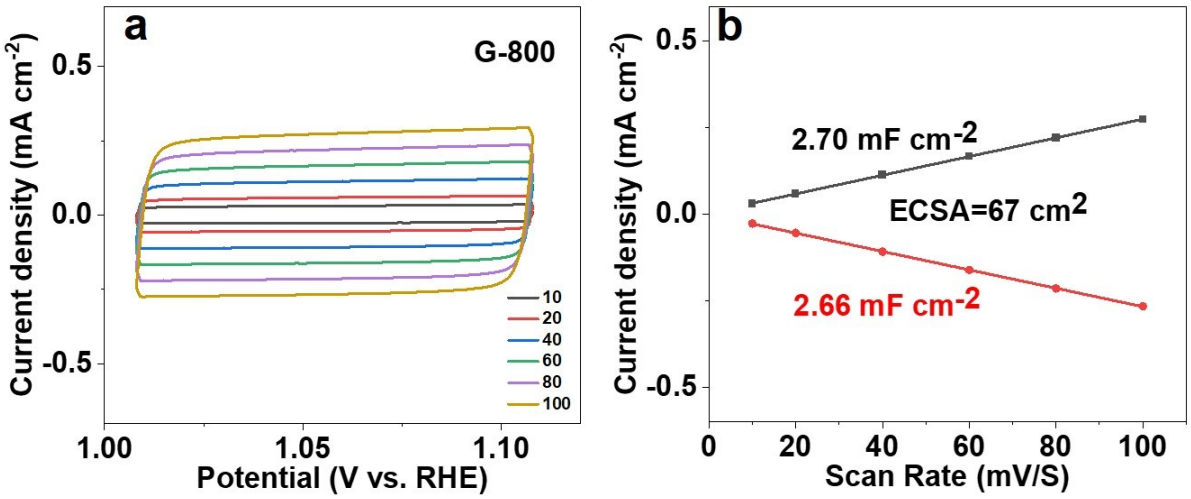

Fig. S9 Double-layer capacitance measurements for determining the electrochemical active surface area for the G-800. (a) CVs measured in a non-Faradaic region at scan rate of 10 mV s^{-1}, 20 mV s^{-1}, 40 mV s^{-1}, 60 mV s^{-1}, 80 mV s^{-1}, and 100 mV s^{-1}. (b) The cathodic (black) and anodic (red) currents measured at 1.059 V vs RHE as a function of the scan rate. The average of the absolute value of the slope is taken as the double-layer capacitance of the electrode.

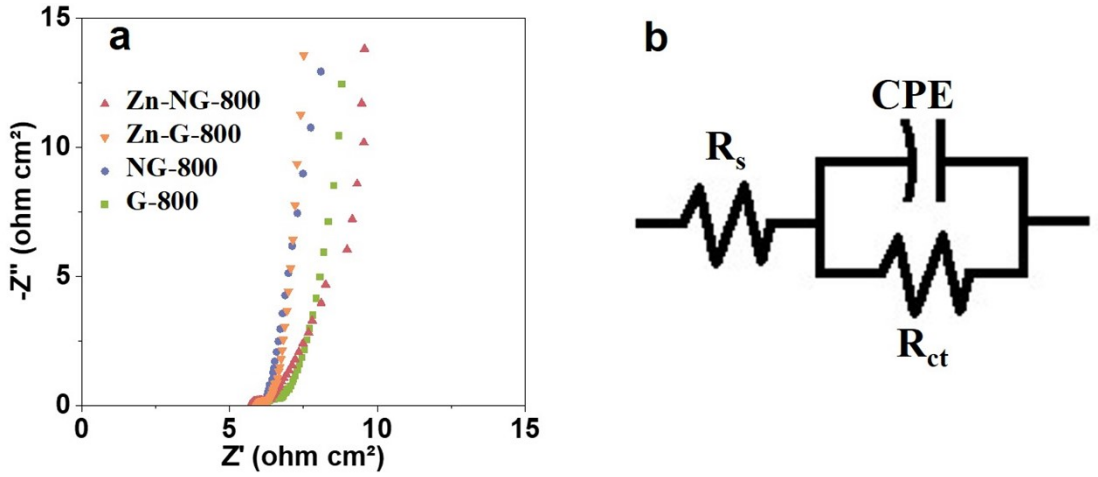

Fig. S10 (a) Nyquist plots of the EIS test for the Zn-NG-800, Zn-G-800, NG-800 and G-800.

(b) The equivalent circuit used for fitting the Nyquist plots.

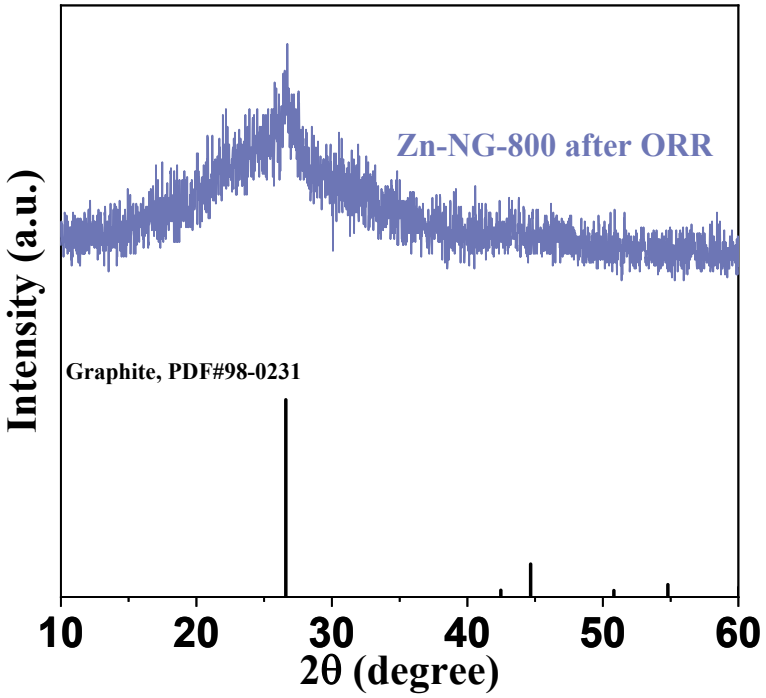

Fig. S11 XRD pattern of the used Zn-NG-800 after ORR test.

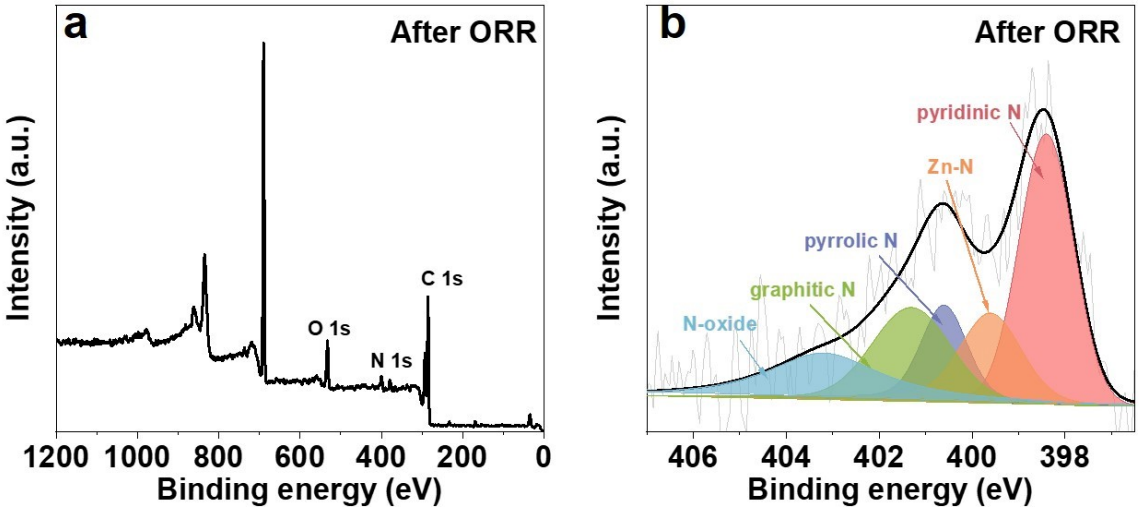

Fig. S12 (a) XPS survey spectrum. (b) XPS spectra of N 1s. The signals at around 685 eV (F 1s), 859 eV (F Auger), and 887 eV (F Auger) are all attributed to the absorbed F ions, because we supported the Zn-NG on a FTO conducting glass with 10*10 cm^2 for the ORR and collected the sample after the reaction.

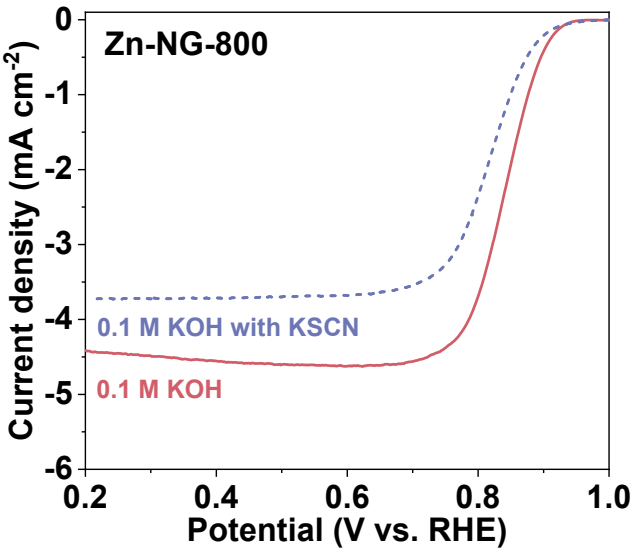

Fig. S13 LSV curves of Zn-NG-800 in 0.1 M KOH with 10 ppm KSCN.

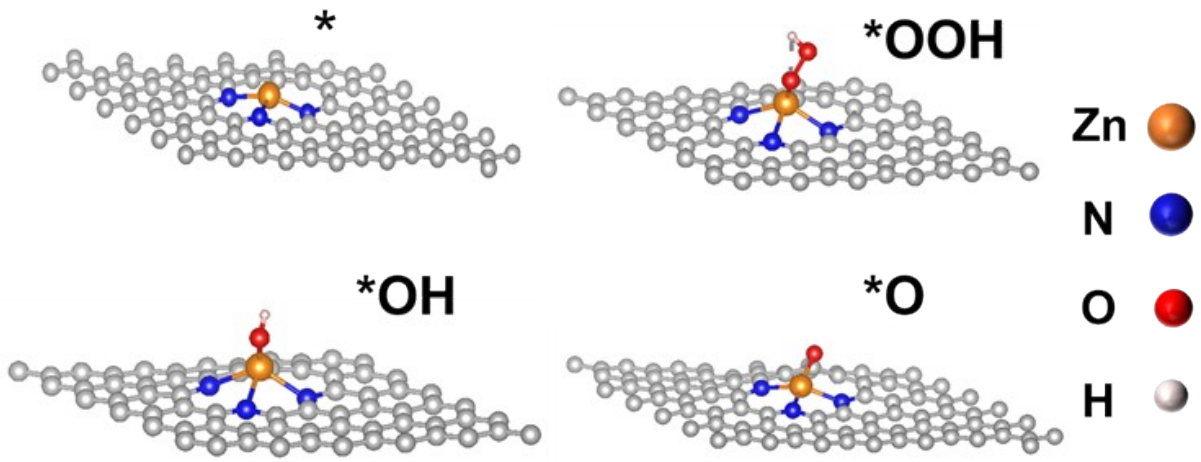

Fig. S14 The stable structure of Zn-N_3G model and the intermediate structures for catalytic ORR. * represents the catalyzed surface.

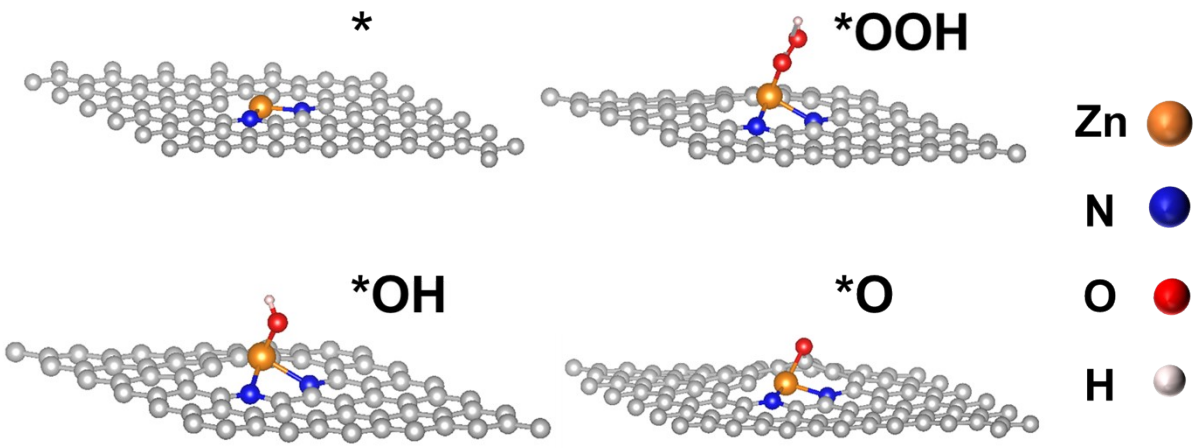

Fig. S15 The stable structure of Zn-N_2G model and the intermediate structures for catalytic ORR. * represents the catalyzed surface.

Table S1. Curve fit parameters of Zn K-edge EXAFS for the Zn-NG

Sample[a]	Path	N[b]	R/Å[c]	σ^2 (10^{-3}Å^2)[d]	ΔE_0/eV	R-factor
Zn-NG	Zn-N	4.18±0.22	1.980±0.014	0.009	3.92±1.61	0.008

[a] S_0^2 was fixed as 0.9. [b] N is the coordination number. [c] R is the distance between absorber and backscatter atoms. [d] σ^2 is the Debye-Waller factor. R-factor is residual factor.

Table S2. Comparison of the ORR performance of SACs in 0.1 M KOH

Catalysts	$E_{1/2}$ (V)	Eon-set potential	Limiting current density (mA cm^{-2})	References
Zn-NG-800	**0.84**	**0.957**	**4.40**	**This work**
Fe_{SA}/NMC-800	0.71	0.930	5.75	[2]
CoSA@NC	0.825	-	5.32	[3]
Fe_3C-FeSA@3DCN	0.835	0.926	5.72	[4]
Fe_1-2D-NOC	0.826	0.985	5.22	[5]
Au SAC CoN@NF	0.767	0.968	-	[6]
Co@SA-NC	0.79	-	4.80	[7]
Co-CMS	0.83	0.88	2.70	[8]

Table S3. Comparison of the performance of SACs-based ZABs

Catalysts	Open-circuit voltage (V)	Peak power density (mW cm^{-2})	Specific capacity (mA h g_{Zn}^{-1})	References
Zn-NG-800	**1.50**	**158**	**730.3**	**This work**
Fe_{SA}/NMC-800	1.45	91	-	[2]
FePc-c–NG-10	1.47	141	750	[9]
M−Fe_2O_3/Fe_{SA}@NC	1.45	155	762	[10]
Co-SAs/N-C/rGO	1.52	141.46	671.94	[11]
Co-N5/DHC.	1.45	160.7	766.2	[12]
Co-W_xC	1.48	188.5	708.1	[13]
NC-30Fe^{3+}-750	1.47	149.1	824	[14]

References

1 S. Ran, J. Qi, X. Dong, H. Huang, M. Qi, W. Dong, P. Zhao, Z. Zhao and J. Yang, Molten NaCl assisted pyrolysis of ZIF-8/PAN electrospun fibers to synthesis 1D cross-linked mesoporous N-rich carbon as oxygen reduction electrocatalysts, *Chem. Eng. J.*, 2023, **463**, 142174.

2 H. Xie, B. Du, X. Huang, D. Zeng, H. Meng, H. Lin, W. Li, T. Asefa and Y. Meng, High Density Single Fe Atoms on Mesoporous N-Doped Carbons: Noble Metal-Free Electrocatalysts for Oxygen Reduction Reaction in Acidic and Alkaline Media, *Small*, 2023, **19**, 2303214.

3 Z. Chen, H. Zheng, J. Zhang, Z. Jiang, C. Bao, C.-H. Yeh and N.-C. Lai, Covalent organic frameworks derived Single-Atom cobalt catalysts for boosting oxygen reduction reaction in rechargeable Zn-Air batteries, *J. Colloid Interface Sci.*, 2024, **670**, 103-113.

4 Q. Yang, R. Liu, Y. Pan, Z. Cao, J. Zuo, F. Qiu, J. Yu, H. Song, Z. Ye and S. Zhang, Ultrahigh-Loaded Fe Single Atoms and Fe_3C Nanoparticle Catalysts as Air Cathodes for High-Performance Zn–Air Batteries, *ACS Appl. Mater. Interfaces*, 2023, **15**, 5720-5731.

5 T. Butburee, J. Ponchai, P. Khemthong, P. Mano, P. Chakthranont, S. Youngjan, J. Phanthasri, S. Namuangruk, K. Faungnawakij, X. Wang, Y. Chen and L. Zhang, General Pyrolysis for High-Loading Transition Metal Single Atoms on 2D-Nitro-Oxygeneous Carbon as Efficient ORR Electrocatalysts, *ACS Appl. Mater. Interfaces*, 2024, **16**, 10227-10237.

6 X. Hu, X. Chen, X. Li and C. Xu, Engineering the Electronic Interaction Between

Single Au Atoms and CoN Through Nitrogen-Coordination Bonding as an Efficient Bifunctional Electrocatalyst for Rechargeable Zn–Air Batteries, *Adv. Funct. Mater.*, 2024, **34**, 2316699.

7 J. Qi, L. Yu, H. Gan, H. Li, S. Guo, D. Wang, Z. Chen, C. Zhao, C. Han and H. M. Cheng, OH-Induced Surface Reconstitution in Single Atoms and Clusters Integrated Electrocatalysts for Self-Adaptive Oxygen Electrocatalysis, *Adv. Funct. Mater.*, 2024, **34**, 2410700.

8 S. Liang, L. C. Zou, L. J. Zheng, F. Li, X. X. Wang, L. N. Song and J. J. Xu, Highly Stable Co Single Atom Confined in Hierarchical Carbon Molecular Sieve as Efficient Electrocatalysts in Metal–Air Batteries, *Adv. Energy Mater.* , 2022, **12**, 2103097.

9 Y. Wu, X. Wang, B. Tian, W. Shuang, Z. Bai and L. Yang, Optimizing reaction intermediate adsorption by engineering the coordination structure of single-atom Fe–N_5–C electrocatalysts for efficient oxygen reduction, *Inorg. Chem. Front.*, 2023, **10**, 4209-4220.

10 F. Zhang, Y. Zhu, Y. Zhong, J. Zou, Y. Chen, L. Zu, Z. Wang, J. J. Hinsch, Y. Wang, L. Zhang, Z. Shao and H. Wang, Tuning the charge distribution and crystal field of iron single atoms via iron oxide integration for enhanced oxygen reduction reaction in zinc-air batteries, *J. Energy Chem.*, 2023, **85**, 154-163.

11 Le Li, Na Li, Jiawei Xia, Shilong Zhou, Xingyue Qian, Fengxiang Yin, Guangyu He and H. Chen, Metal–organic framework-derived Co single atoms anchored on N-doped hierarchically porous carbon as a pH-universal ORR electrocatalyst for Zn–air batteries, *J. Mater. Chem. A*, 2023, **11**, 2291–2301

12 L. Zhao, Z. Zhang, Z. Zhu, P. Li, J. Jiang, T. Yang, P. Xiong, X. An, X. Niu, X. Qi, J.

S. Chen and R. Wu, Integration of atomic Co-N_5 sites with defective N-doped carbon for efficient zinc-air batteries, *Chin. J. Catal.*, 2023, **51**, 216-224.

13 H. Li, W. Wang, S. Xue, J. He, C. Liu, G. Gao, S. Di, S. Wang, J. Wang, Z. Yu and L. Li, Superstructure-Assisted Single-Atom Catalysis on Tungsten Carbides for Bifunctional Oxygen Reactions, *J. Am. Chem. Soc.* , 2024, **146**, 9124-9133.

14 Y. Sha, F. Moissinac, M. Zhu, K. Huang, H. Guo, L. Wang, Y. Liu, L. Li, A. Thomas and Z. Liu, Laser Synthesis of Nonprecious Metal-Based Single-Atom Catalysts for Oxygen Reduction Reaction, *ACS Appl. Mater. Interfaces* 2023, **15**, 51004-51012.